Article │ Received 30 May 2024; Accepted 13 August 2024; Published 20 August 2024
https://doi.org/10.55092/am20240011

Advanced hydrogel strain sensors from non-aqueous resins via UV-cured 3D printing

Binbin Guo[1,2,†], Xiaoteng Chen[1,†], Hui Ying Yang[2,*] and Jiaming Bai[1,*]

[1] Shenzhen Key Laboratory for Additive Manufacturing of High-performance Materials, Department of Mechanical and Energy Engineering, Southern University of Science and Technology, Shenzhen 518055, China

[2] Pillar of Engineering Product Development, Singapore University of Technology and Design, 8 Somapah Road, Singapore 487372, Singapore

† These authors contributed equally to this work.

* Corresponding authors; E-mails: yanghuiying@sutd.edu.sg (H.Y.Y.); baijm@sustech.edu.cn (J.B.).

Abstract: Hydrogel-based strain sensors have attracted considerable interest in real-time healthcare and motion detection because of their remarkable flexibility, extensibility, and skin-like compatibility. To reduce the cost and accelerate the preparation of hydrogels, digital light processing (DLP) 3D printing technology presents a promising strategy. However, current photosensitive resin systems primarily use aqueous slurries, which slow down the 3D printing process due to high water content. Herein, we selected three non-aqueous resins for hydrogel preparation and adopted a two-step strategy involving UV curing through 3D printing followed by water spraying. We systematically investigated the curing kinetics and rheological properties of resins, as well as water absorption behavior, mechanical characteristics, and tensile-fracture mechanisms of the resulting hydrogels. Our findings established the poly (Nacryloylmorpholine) hydrogel as the reliable substrate material, NaCl aqueous solution was sprayed to endow the hydrogel with promising ionic conductivity and sensing properties. This work paves the way for the rapid fabrication of 3D printed ionically conductive hydrogels from non-aqueous resins.

Keywords: strain sensor; 3D printing; hydrogel; non-aqueous resins

1. Introduction

Hydrogels are soft materials characterized by a unique three-dimensional (3D) network structure formed through the physical or chemical cross-linking of polymers [1–3]. Owing to its exceptional properties, such as high stretchability and biocompatibility, hydrogels have

found extensive applications in the application of flexible wearable strain sensors [4,5]. It is noteworthy that the fabrication of hydrogel-based flexible strain sensors has predominantly relied on conventional methods, including freeze-thaw cycles and in-situ polymerization [6,7]. These approaches are not only intricate and time-consuming but also necessitate mold opening and demolding processes, significantly hindering the large-scale production of flexible strain sensors. Consequently, there is an urgent need to develop efficient and convenient fabrication methods to expedite the industrial production of flexible strain sensors. 3D printing, also known as additive manufacturing, is an advanced fabrication technique that constructs 3D solid objects by successively depositing material layers based on computer-designed 3D models [8,9]. Compared to traditional manufacturing methods, 3D printing offers notable advantages in terms of efficiency, convenience, and customization potential [10,11].

As one of the most cutting-edge 3D printing technologies, digital light processing (DLP) has been extensively utilized to fabricate polymeric products with high precision and rapid production speeds [12,13]. This technology has been extensively applied across various fields, demonstrating significant potential in the fabrication of flexible strain sensors. For example, Xiang-Yu Yin *et al.* constructed ionically conductive hydrogels using acrylamide-based slurries by DLP 3D printing, and the integrated sensor exhibited high sensitivity and low detection limit [14]. Inspired by this, Zhaolong Wang and coworkers adopted acrylamide-based slurries to prepare ultrastretchable and hyper-antifreezing conductive hydrogel sensors by DLP 3D printing [15]. Additionally, acrylic acid-based slurries were also widely utilized to fabricate hydrogel-based strain sensors by DLP 3D printing [16–18]. However, the current hydrogel precursors commonly used in this process are predominantly water-based slurries, which pose several technical challenges due to high water content. Firstly, the presence of water inhibits the photopolymerization reaction [19]. Since water does not participate in the UV curing reaction, higher intensity UV light and longer exposure times are required to achieve the desired curing of hydrogels, significantly prolonging the printing process. Therefore, the exploitation and application of non-aqueous resins for the fast fabrication of hydrogel-based strain sensors has become an urgent priority.

Inspired by the molecular structures of acrylic acid and acrylamide commonly used in traditional hydrogels, three photosensitive resins of N-acryloylmorpholine (ACMO), hydroxyethyl methacrylate (HEMA), and polyethylene glycol diacrylate (PEGDA) were selected for DLP 3D printing (Figure 1). The molecular formulas of ACMO and HEMA have short carbon chains, resembling acrylamide and acrylic acid. ACMO and HEMA contain carbonyl, ether, and tertiary amine/hydroxyl groups, which readily form hydrogen bonds with hydroxyl groups in water, indicating that cured ACMO and HEMA parts have the potential for water absorption. Compared with ACMO and HEMA, PEGDA has been considered an ideal material for preparing bio-based hydrogels [20,21]. An approach involving pre-curing through 3D printing followed by water spraying was proposed for the preparation of hydrogels, aimed at expediting the fabrication process. The curing kinetics and rheological properties of three non-aqueous resins were systematically studied, along with the water absorption behavior, mechanical characteristics, and associated tensile-fracture mechanisms of the corresponding hydrogels. As a proof of concept, a NaCl aqueous solution was applied

to impart the P(ACMO) hydrogel with promising ionic conductivity and sensing properties. Exploring the design principles of ionically conductive hydrogels derived from non-aqueous resins lays the groundwork for future studies on the rapid fabrication of wearable strain sensors.

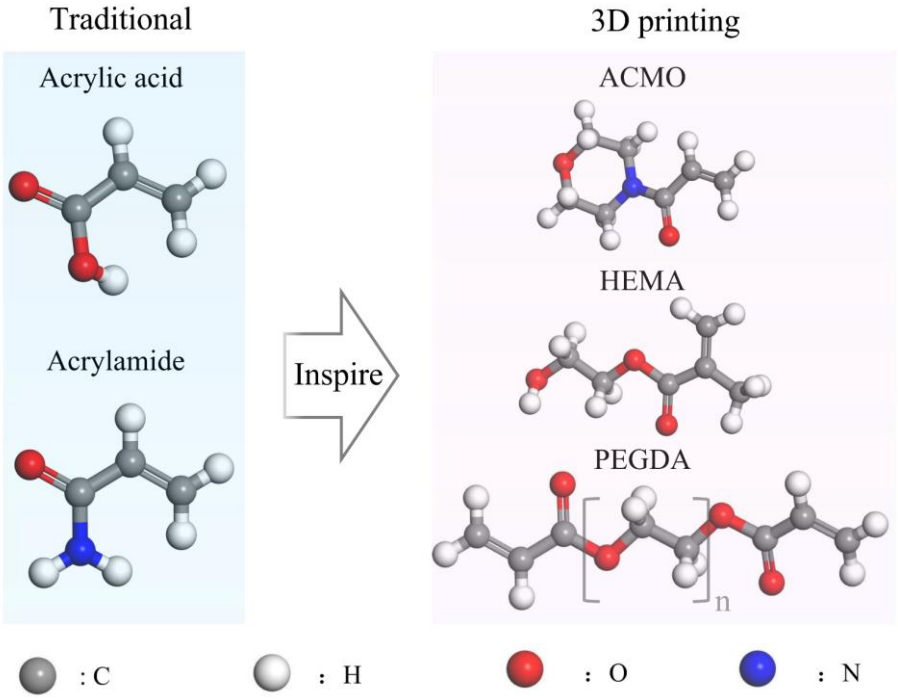

Figure 1. Molecular formulas of the acrylic acid, acrylamide, ACMO, HEMA, and PEGDA.

2. Methods

2.1. Materials

ACMO, HEMA, PEGDA (molecular weight 600), photo-initiator 2,4,6-trimethylbenzoyl diphenylphosphine oxide (TPO), and sodium chloride (NaCl) (purity≥99.5%) were purchased from Nikko Koichi Chemical Co., Ltd., Mitsubishi Rayon Corporation of Japan, Shanghai Yinchang New Material Co., Ltd., Shanghai Aladdin Biochemical Technology Co., Ltd., and Shantou Xilong Science Co., Ltd., respectively. All chemicals were utilized as received without undergoing additional purification.

2.2. Preparation of P(ACMO), P(HEMA), and P(PEGDA) hydrogels, and P(ACMO)/NaCl hydrogel strain sensor

Initially, 100 g of ACMO, HEMA, and PEGDA resins were measured and individually placed into three distinct containers. Subsequently, 1 g of TPO was added to each container. The containers were subjected to ultrasonication for 20 min within an ultrasonic cleaning device (SB-5200DT, 200 W, Ningbo, China) to produce ACMO, HEMA, and PEGDA resins. The resins were then UV-polymerized through a DLP printer (Asiga, Pico 2). The UV light wavelength, layer thickness, and number of cured layers were set at 405 nm, 25 μm, and 3 layers, respectively. The exposure parameters differed for each resin: ACMO and PEGDA

resins were exposed to an intensity of 5 mW/cm^2 for 3 s, while the HEMA resin required an intensity of 50 mW/cm^2 for 30 s. Following printing, the poly(ACMO), poly(HEMA), and poly(PEGDA) (abbreviated as P(ACMO), P(HEMA), and P(PEGDA)) components underwent ethanol cleaning. The 3D printed specimens were UV cured for 10 min using a UV curing machine. Finally, the P(ACMO), P(HEMA), and P(PEGDA) parts underwent water absorption treatment to yield P(ACMO), P(HEMA), and P(PEGDA) hydrogels, as shown in Figure 2. Concerning the preparation of the P(ACMO)/NaCl hydrogel strain sensor, the P(ACMO) component was NaCl aqueous solution sprayed. To prevent the dehydration of the hydrogel-based strain sensor, the P(ACMO)/NaCl hydrogel was encapsulated between two layers of 3M tapes.

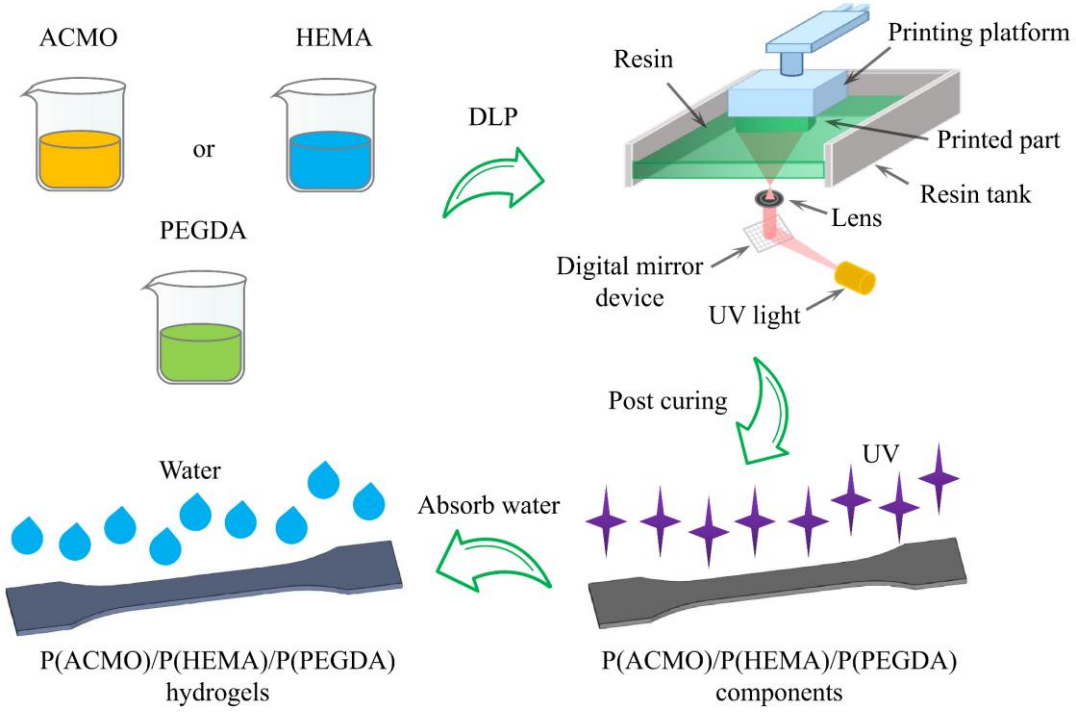

Figure 2. Schematic illustration of the preparation of P(ACMO), P(HEMA), and P(PEGDA) hydrogels.

2.3. Characterization

The assessment of curing depth for the ACMO, HEMA, and PEGDA resins was conducted using a DLP printing apparatus (Asiga, Pico 2). The process entailed loading individual resin into a resin tank, followed by exposure to a single UV illumination with adjustable energy doses, excluding the use of the printing platform. Afterward, the cured components were extracted and subjected to testing using a micrometer caliper. The Beer-Lambert equation was employed to illustrate the impact of exposure dose on curing depth [22]:

$$C_d = S_d \ln E - S_d \ln E_c \quad (1)$$

where C_d represents the curing depth, S_d denotes the sensitivity of the suspension, E stands for the exposure energy dose, and E_c refers to the critical exposure energy dose. Viscosities of the ACMO, HEMA, and PEGDA resins were measured and recorded as a function of shear rate

ranging from 5.36 S^{-1} to 100 S^{-1} using a rotational rheometer MCR-92 (Anton Paar, Australia). The relative weight change of DLP-printed samples before and after absorbing water/NaCl aqueous solution was calculated employing an electronic scale by the following formula:

$$\frac{\Delta m}{m_0}(\%) = \frac{m - m_0}{m_0} \times 100 \quad (2)$$

where m_0 and m are the weights before and after spraying water/NaCl aqueous solution, respectively. The mechanical characterization was carried out on a universal testing machine (Guangzhou Precision Control Testing Instrument Co., Ltd., XLD-100E, China). For the uniaxial tensile testing, the tensile speed was 10 mm/min. During the successive tensile tests (100 cycles) with a 100% strain on the P(ACMO)/NaCl hydrogel strain sensor, the tensile speed was 100 mm/min. The Electrochemical impedance spectroscopy (EIS) was conducted over the frequency range of 0.1 Hz to 1 MHz utilizing an electrochemical workstation (VMP3, Biologic). The ionic conductivity of the hydrogel was calculated by:

$$\sigma = \frac{l}{RA} \quad (3)$$

where σ represents the ionic conductivity of the hydrogel, and l, R, and A correspond to the thickness, bulk resistance, and test area of the hydrogel, respectively. The relative resistance change of the P(ACMO)/NaCl hydrogel sensors was recorded on a Keithley DMM7510 multimeter, which was measured using the following formula:

$$\frac{\Delta R}{R_0}(\%) = \frac{R - R_0}{R_0} \times 100 \quad (4)$$

where R_0 and R represent the resistance before and after applying strain, respectively. Regarding the tensile cycle test, the P(ACMO)/NaCl hydrogel strain sensors were fitted on a homemade tensile equipment to generate various strains. To detect various human motions, the sensors were fixed on the human finger and wrist. NIH-3T3 cells were cultured in MEM complete medium, consisting of 90% glucose-free MEM (GIBCO), 10% (v/v) fetal bovine serum (FBS, GIBCO), and 1% (v/v) penicillin/streptomycin (10,000 U/mL, GIBCO). The cells were maintained at 37 °C in a humidified atmosphere with 5% (v/v) CO_2. A live/dead staining assay was performed using a Calcein-AM/PI double stain kit. The cells were plated in 96-well culture plates at a density of 1×10^4 cells per well, and the P(ACMO) hydrogel sample was added to the respective wells. After 1, 3, and 7 days' incubation, the cells were washed twice with PBS, respectively. Then, 100 μL of Calcein-AM/PI double stain detection working solution was added according to the manufacturer's instructions. After incubating for 30 minutes, the cells were washed twice with PBS. Finally, live cells stained with Calcein-AM ($\lambda_{ex}/\lambda_{em} = 490$ nm/515 nm) and dead cells stained with PI ($\lambda_{ex}/\lambda_{em} = 535$ nm/617 nm) were observed using a confocal microscope.

3. Result and discussion

To investigate the photocuring features of various resins, the cure depth of the ACMO, HEMA, and PEGDA resins are shown in Figure 3(a). The critical exposure energy dose (E_c) of the ACMO, HEMA, and PEGDA resins was 11.6, 1288.8, and 10.9 mJ/cm², respectively.

The higher E_c of the HEMA than that of the ACMO and PEGDA was attributed to the presence of CH_3 donor groups on the double bonds of HEMA, which enhanced the electron density of the double bonds, thus reducing their susceptibility to radical attack and impeding the formation of active radicals during polymerization (Figure 1). This indicated that the photocuring properties of the ACMO and PEGDA resins surpass those of the HEMA resin, rendering them more suitable for photocuring 3D printing applications. For P(ACMO), the curing time for each layer was 3 s and the printing duration of the whole sample was approximately 1.5 min, which was significantly shorter than that of other DLP-printed hydrogels [15–18].

In addition to photopolymerization characteristics, rheological properties of photosensitive resins are also critical attributes in DLP 3D printing. In upward photopolymerization 3D printing, after each layer of photosensitive resin is cured, the printing platform ascends and then descends, maintaining a constant layer thickness with the release film [23]. Lower resin viscosity enables rapid flow, filling the gap between the printing platform and the release film, thus facilitating the curing of the next resin layer. Viscosities of different resins at shear rates ranging from 5.4 S^{-1} to 100 S^{-1} were measured using a rotational rheometer (Figure 3(b)). Note that the order of viscosity from lowest to highest among the three resins was HEMA < ACMO < PEGDA, and the viscosity of the ACMO and HEMA resins at various shear rates was below 20 mPa·s, suggesting promising rheological properties.

Figure 3(c) displays images of the P(ACMO), P(HEMA), and P(PEGDA) specimens. Due to the higher exposure energy required for curing the HEMA resin, over-curing was prone to occur at high energy densities, resulting in lower precision of the P(HEMA) part. In contrast, the P(ACMO) and P(PEGDA) components demonstrated higher precision in their contours. To investigate the water absorption capacity of the P(ACMO), P(HEMA), and P(PEGDA) parts, each specimen was first placed into a beaker, then an excess of water was added, and it was allowed to stand for 30 min before being removed. Subsequently, relative mass changes ($\Delta m/m_0$) were measured using an electronic balance. As shown in Figure 3(d), the P(ACMO) part dissolved in water after 30 min of standing, while the structures of the P(HEMA) and P(PEGDA) components remained intact. The $\Delta m/m_0$ of the P(HEMA) and P(PEGDA) specimens were 99.6 ± 5.01% and 55.5 ± 2.11%, respectively. The water absorption performance among the three specimens followed the order from smallest to largest: P(PEGDA) < P(HEMA) < P(ACMO).

To explain the different water absorption characteristics of the P(ACMO), P(HEMA), and P(PEGDA) components, the molecular structures and internal crosslinking mechanisms of the three specimens were analyzed. As shown in Figure 3(e), ACMO featured a single C=C bond that did not participate in chemical crosslinking during polymerization [24]. Instead, it contributed to chain segment entanglement. Additionally, the rigid ring structure present in ACMO hindered the entanglement of P(ACMO) segments during polymerization. Due to the presence of hydrophilic groups such as ether bonds and carbonyl groups on the P(ACMO) chains, water molecules were able to penetrate and cause segment untangling until the P(ACMO) component dissolved. Similar to ACMO, HEMA contained a single C=C bond, which theoretically did not form chemical crosslinks during polymerization. Compared with ACMO, HEMA contained a hydroxyl group, which readily formed hydrogen bonds with

carbonyl and ether groups, resulting in physical crosslinking during polymerization [25]. Despite the presence of hydrophilic groups such as ether and carbonyl groups in the P(HEMA) chains, water molecules encountered challenges in disrupting the physical crosslinking, thereby preserving the structural stability of the P(HEMA) part. Unlike ACMO and HEMA, PEGDA contained two C=C bonds, leading to chemical crosslinking during polymerization [26]. Water molecules encountered heightened difficulty in disrupting the chemical crosslinking among P(PEGDA) segments, consequently preserving the structural stability of the P(PEGDA) component.

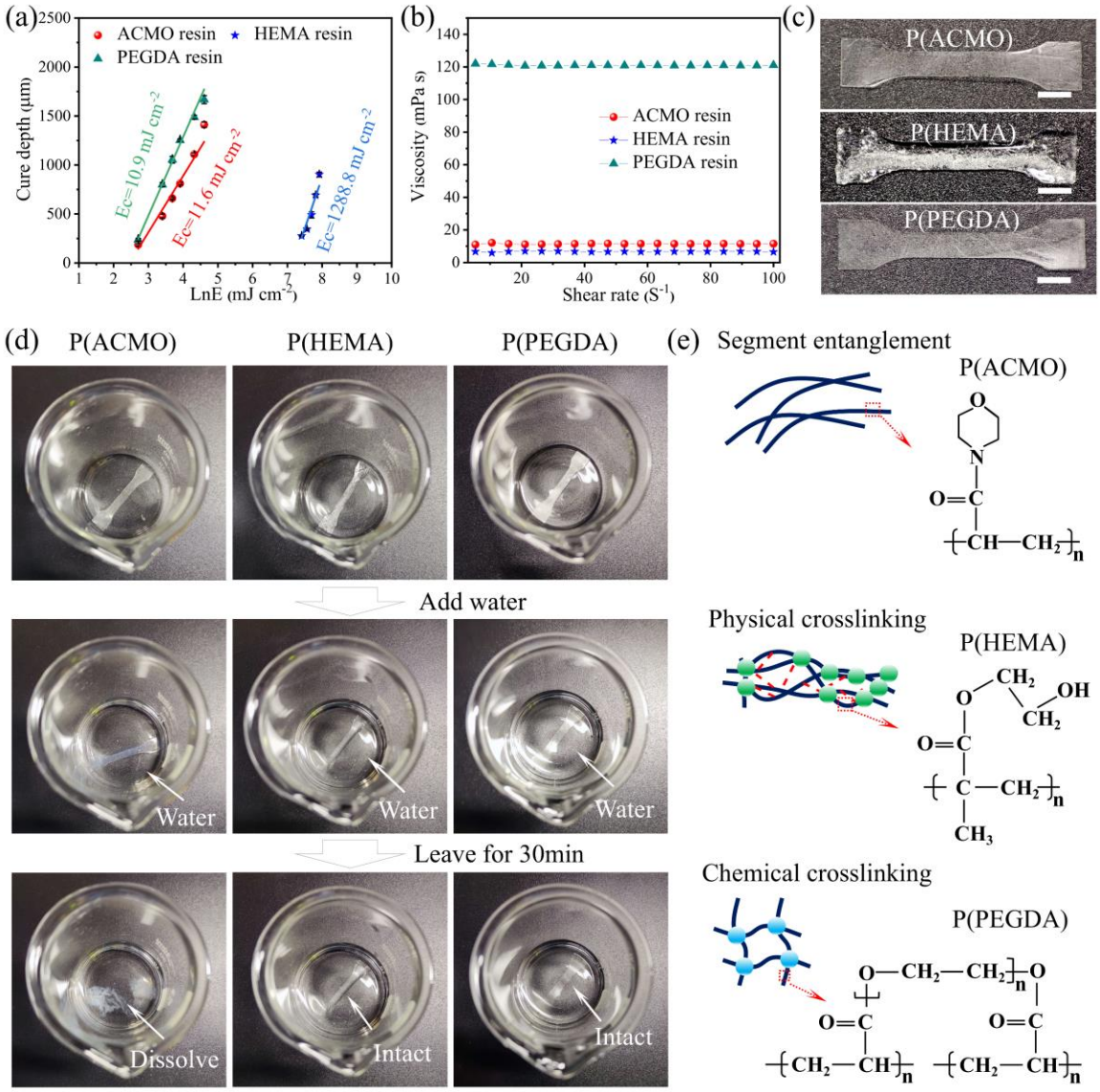

Figure 3. (a) Linear fitting of cure depth within various logarithmic exposure dose of ACMO, HEMA, and PEGDA resins. **(b)** Shear rate-viscosity relationship of the ACMO, HEMA, and PEGDA resins. **(c)** Digital photographs, **(d)** water absorption property, and **(e)** molecular formulas and internal crosslinking mechanism of the P(ACMO), P(HEMA), and P(PEGDA) parts. Scale bars: 5 mm.

To examine the effect of water concentration on the stability of the P(ACMO) hydrogel, different $\Delta m/m_0$ values (50, 75, 100, 125, and 150 wt %) of the P(ACMO) part were tested (Figure 4(a)). As illustrated in Figure 4(b), negligible dissolution and promising stretchability were observed in the P(ACMO) hydrogel at a $\Delta m/m_0$ of 100 wt %, indicating excellent structural stability and weather resistance. It is noted that when the $\Delta m/m_0$ of the specimen increased to 125 wt %, the P(ACMO) part began to dissolve (Figure 4(b)). Therefore, for the preparation of P(ACMO) hydrogel, its $\Delta m/m_0$ should not have exceeded 100 wt %.

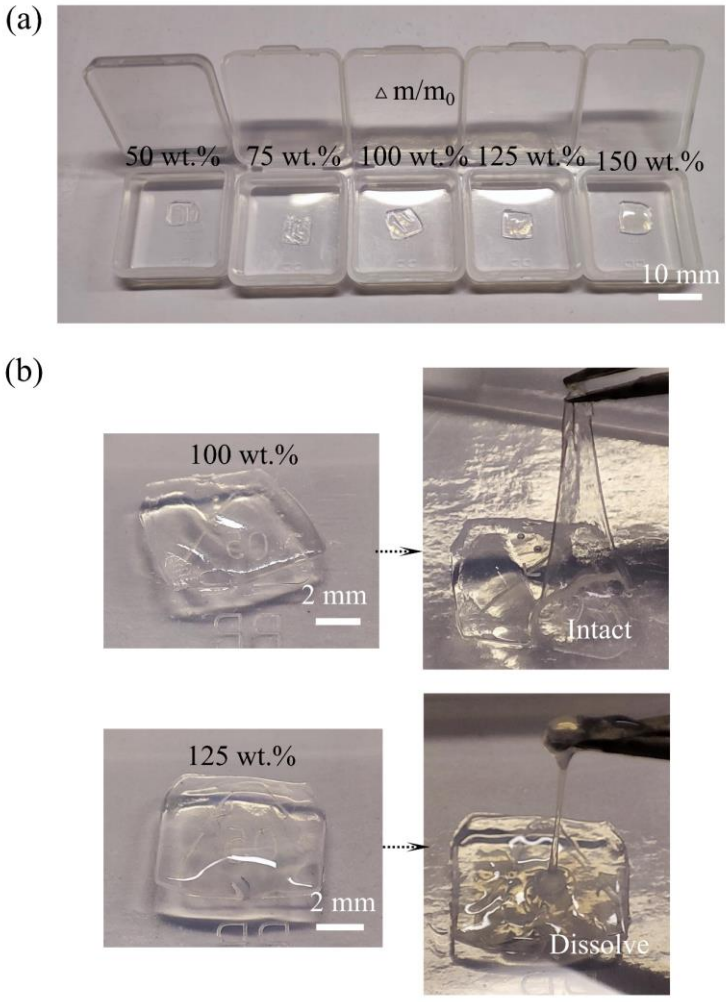

Figure 4. (a) Digital photographs of the P(ACMO) hydrogel with various relative weight changes (50, 75, 100, 125, and 150 wt %). **(b)** Magnified images of the P(ACMO) hydrogel with relative weight changes of 100 and 125 wt %.

After investigating the water absorption properties of the P(ACMO), P(HEMA), and P(PEGDA) parts, hydrogels with different water concentration were prepared. The water content in the hydrogels was determined based on the $\Delta m/m_0$ of the specimen. For instance, when the $\Delta m/m_0$ of the specimen was 25, 50, 75, and 100 wt %, the corresponding water content in the hydrogels was 20, 33.3, 42.9, and 50 wt %, respectively.

The mechanical properties of the P(ACMO), P(HEMA), and P(PEGDA) hydrogels were characterized. The stress-strain curves of the P(ACMO) hydrogels with various water content

are shown in Figure 5(a), and the corresponding mechanical parameters are presented in Figure 5(b). As the water content increased from 20 to 33.3, 42.9, and 50 wt %, the Young's modulus and yield strength of the P(ACMO) hydrogels gradually decreased. Conversely, the elongation at break of the P(ACMO) hydrogels gradually increased. Notably, with an increase in water content to 42.9 wt %, the Young's modulus, yield strength, and elongation at break of the P(ACMO) hydrogel remained essentially unchanged, at 0.02 ± 0.009 MPa, 0.09 ± 0.056 MPa, and 1504.3 ± 106.70%, respectively.

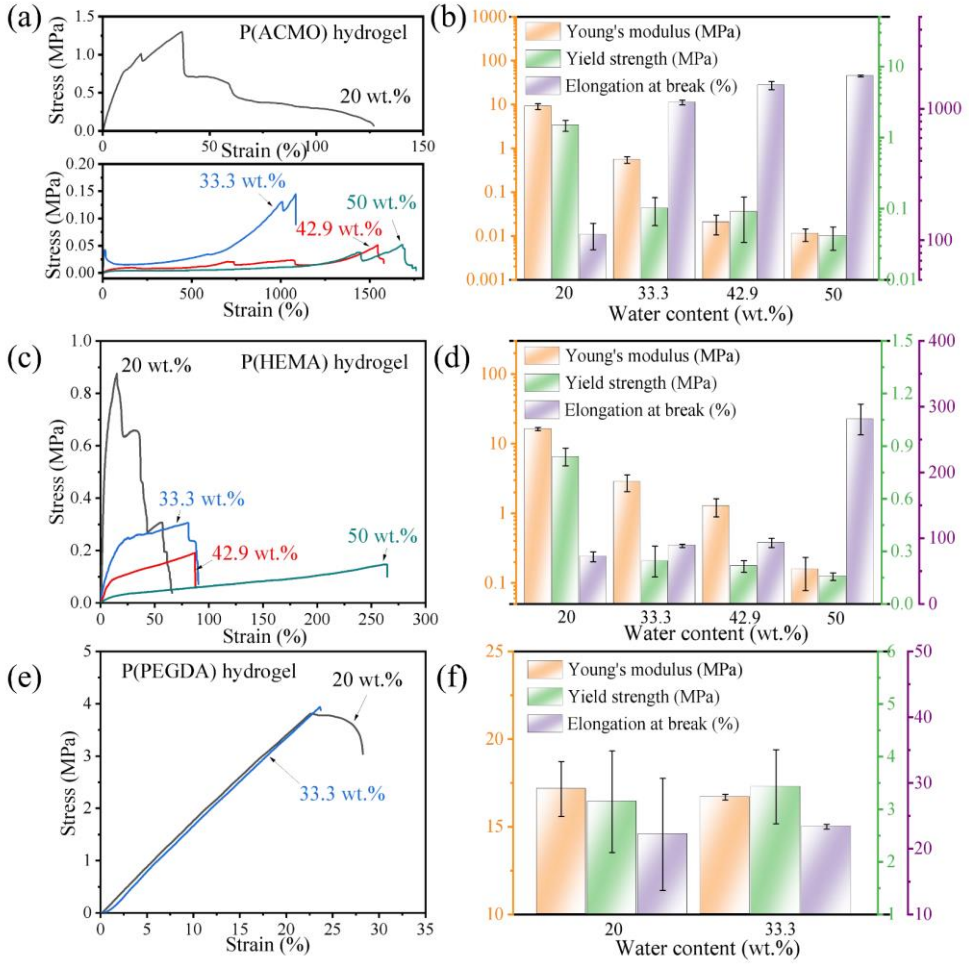

Figure 5. Stress-strain curves and mechanical parameters of the **(a, b)** P(ACMO), **(c, d)** P(HEMA), and **(e, f)** P(PEGDA) hydrogels.

The stress-strain curves and corresponding mechanical parameters of the P(HEMA) hydrogels with different water contents are shown in Figures 5(c) and 5(d), respectively. P(HEMA) hydrogels exhibited a similar trend in mechanical performance variation to the P(ACMO) hydrogels. With an increase in water content, the Young's modulus and yield strength of the P(HEMA) hydrogels gradually decreased, while the elongation at break increased. When the water content reached 50 wt %, the Young's modulus, yield strength, and elongation at break of the P(HEMA) hydrogel were 0.15 ± 0.078 MPa, 0.16 ± 0.021 MPa, and 280.5 ± 23.33%, respectively. Note that when the water content was kept at 42.9 wt %, the modulus and strength of the P(ACMO) hydrogel were lower than those of the

P(HEMA) hydrogel, while the elongation at break was significantly higher than that of the P(HEMA) hydrogel.

The stress-strain curves and corresponding mechanical parameters of P(PEGDA) hydrogels with different water contents are shown in Figures 5(e) and 5(f), respectively. Unlike P(ACMO) and P(HEMA) hydrogels, the mechanical properties of P(PEGDA) hydrogels remained essentially unchanged with increasing water content. Specifically, when the water content was 33.3 wt %, the Young's modulus, yield strength, and elongation at break of P(PEGDA) hydrogels were 16.7 ± 0.16 MPa, 3.4 ± 0.70 MPa, and 23.4 ± 0.35%, respectively. The order of mechanical stretchability among the three hydrogels was from smallest to largest: P(PEGDA) < P(HEMA) < P(ACMO).

Figure 6 depicts the images of the P(ACMO) and P(HEMA) hydrogels with a water content of 42.9 wt % and P(PEGDA) hydrogel with a water content of 33.3 wt %. It is noteworthy that the P(ACMO) hydrogel could be stretched from 10.9 mm to 177.6 mm, demonstrating excellent mechanical stretchability. Therefore, in the field of flexible strain sensors with high strain requirements, P(ACMO) hydrogel exhibited greater advantages.

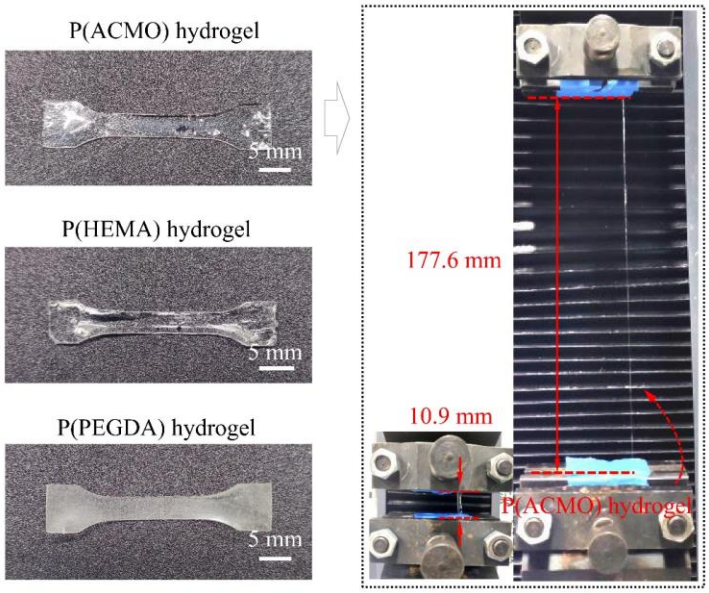

Figure 6. Photographs of the P(ACMO), P(HEMA), and P(PEGDA) hydrogels and demonstration of the stretchable process of the P(ACMO) hydrogel.

P(ACMO), P(HEMA), and P(PEGDA) hydrogels exhibited different mechanical properties due to their distinct molecular structures. As shown in Figure 7(a), P(ACMO) chains contained ether, carbonyl, and tertiary amine groups, enhancing the hydrophilicity of the P(ACMO) part [27]. Water molecules easily penetrated into the interior of the P(ACMO) part, causing untangling of polymer chains. Meanwhile, hydroxyl groups in water could form hydrogen bonds with oxygen and nitrogen atoms in ether, carbonyl, and tertiary amine groups on P(ACMO) chains. For the P(ACMO) hydrogel, its primary crosslinking mechanism involved hydrogen bonding interactions between segments and water, rather than entanglement of segments. As the applied stress increased gradually, the hydrogen bonds

between P(ACMO) and water molecules broke to release stress. Simultaneously, the broken hydrogen bonds could recombine. The reversible breaking/recombining of hydrogen bonds between P(ACMO) and water molecules endowed the P(ACMO) hydrogel with excellent mechanical stretchability.

As shown in Figure 7(b), similar to P(ACMO) hydrogel, P(HEMA) hydrogel contained numerous hydrogen bonds internally, primarily formed between water molecules and hydroxyl, ether, and carbonyl groups on the P(HEMA) segments. In contrast to the P(ACMO) hydrogel, the predominant crosslinking mechanism in the P(HEMA) hydrogel was physical crosslinking between segments. Under low stress, the hydrogen bonds between P(ACMO) and water molecules broke to release stress, endowing the P(HEMA) hydrogel with stretchability. As the applied stress gradually increased, the physical crosslinking networks within the P(HEMA) hydrogel served as stress concentration points, resulting in gel failure once the hydrogel reached its rupture threshold.

As shown in Figure 7(c), unlike P(ACMO) and P(HEMA) hydrogels, the primary crosslinking mechanism of the P(PEGDA) hydrogel was chemical crosslinking. With an increase in tensile stress, the internal chemical crosslinking networks of the P(PEGDA) hydrogel acted as stress concentration points, leading to gel failure. Consequently, the P(PEGDA) hydrogel exhibited higher Young's modulus and yield strength, and lower elongation at break compared to the P(ACMO) and P(HEMA) hydrogels.

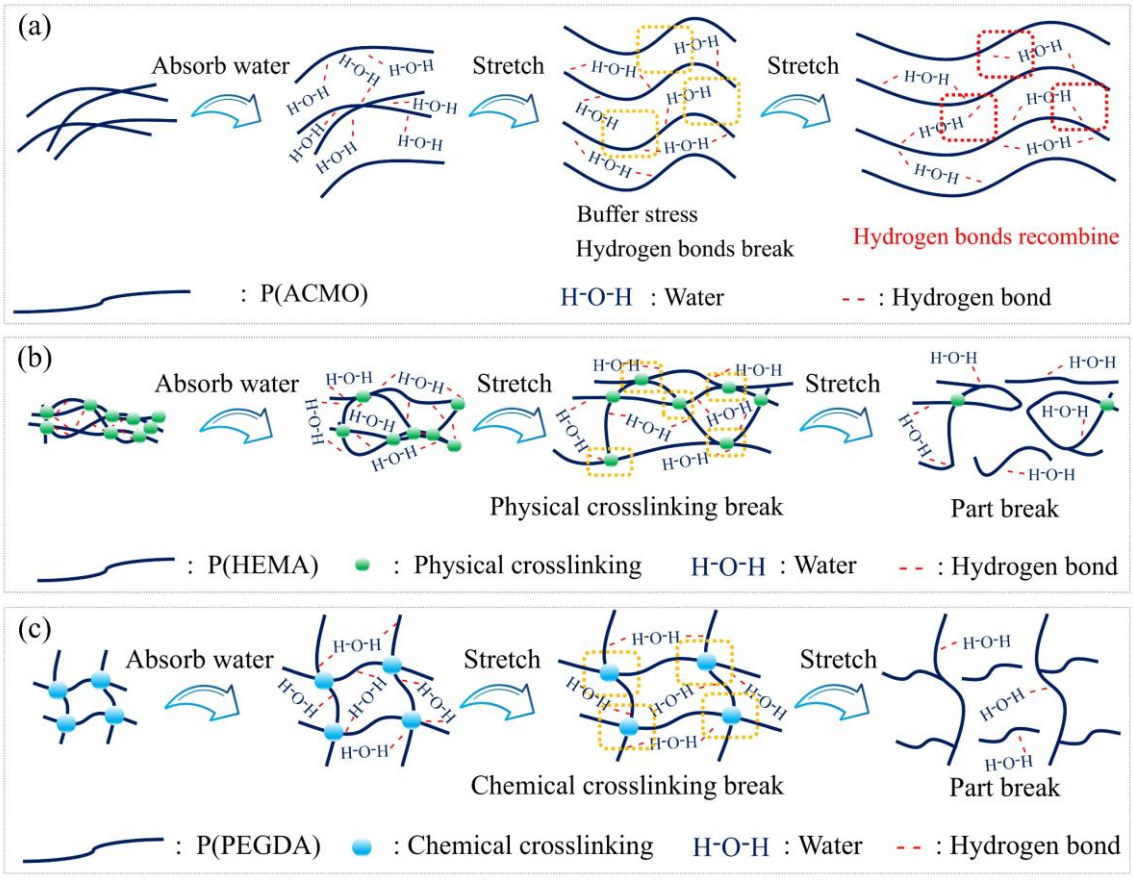

Figure 7. Schematic illustration of the water absorption and stretchable process of the **(a)** P(ACMO), **(b)** P(HEMA), and **(c)** P(PEGDA) parts.

After investigating the tensile-fracture mechanisms of different types of hydrogels, the following radical point is the application of the P(ACMO) hydrogel. As part of the experimental validation, the P(ACMO) component was sprayed by a 5 wt % NaCl aqueous solution to maintain the hydrogel's water content at 42.9 wt %. The mechanical property of the P(ACMO)/NaCl hydrogel was characterized using a universal testing machine with a tensile speed of 10 mm/min¹. Figure 8(a) presents the stress-strain curve of the P(ACMO)/NaCl hydrogel. The hydrogel exhibited excellent tensile properties, with a Young's modulus, yield strength, and elongation at break of 0.04 ± 0.007 MPa, 0.20 ± 0.014 MPa, and 1045.1 ± 153.23%, respectively.

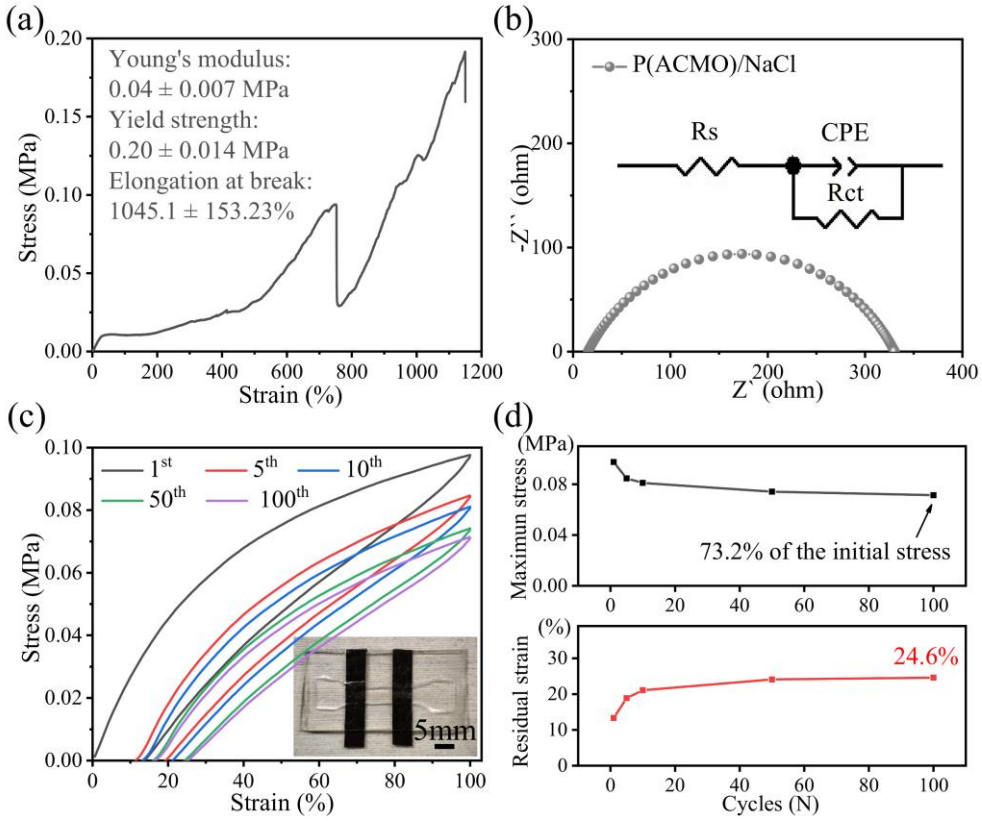

Figure 8. (a) Stress-strain curve and **(b)** EIS of the P(ACMO)/NaCl hydrogel. The inset shows an equivalent circuit. **(c)** Successive tensile test of the P(ACMO)/NaCl hydrogel without any residence time. The inset shows the image of the P(ACMO)/NaCl sensor. **(d)** The maximum stress and residual strain versus tensile cycles of the P(ACMO)/NaCl hydrogel strain sensor with the strain of 100%.

The electrochemical impedance spectra (EIS) of the P(ACMO)/NaCl hydrogel were collected, and Figure 8(b) shows the corresponding Nyquist plot. Furthermore, an equivalent circuit was modeled, in which Rs represented the resistance of the solution, CPE indicated a constant phase element, and Rct represented the resistance to charge transfer. Rs and Rct of the hydrogel were 15.0 ± 2.42 and 247.5 ± 61.10 Ω, respectively. The ionic conductivity of the P(ACMO)/NaCl hydrogel was calculated to be 0.08 ± 0.016 S/m.

To prevent dehydration and enhance the resilience of the P(ACMO)/NaCl hydrogel during use, it was encapsulated with 3M tape, as depicted in Figure 8(c). To assess the elasticity properties of the P(ACMO)/NaCl hydrogel strain sensor, continuous cyclic tensile tests were performed at a strain of 100% without any pause between cycles. As shown in Figure 8(c), the strain sensor exhibited a significant hysteresis loop during the first loading-unloading cycle, with an initial residual strain of 13.3%, demonstrating promising elasticity. This level of residual strain was similar to that documented in the literature for most elastomer, ionogel, and hydrogel-based strain sensors [28–32]. As the tensile cycles progressed, there was a slight decrease in tensile strength, indicating delayed recovery of the strain sensor. Notably, similar hysteresis areas were observed in the subsequent 99 tensile cycles. Furthermore, the strain sensor retained maximum stress (73.2%) and residual strain (24.6%) after 100 tensile cycles, demonstrating good fatigue resistance (Figure 8(d)). This potential fatigue resistance contributed to enhancing the cycling stability of the hydrogel strain sensor.

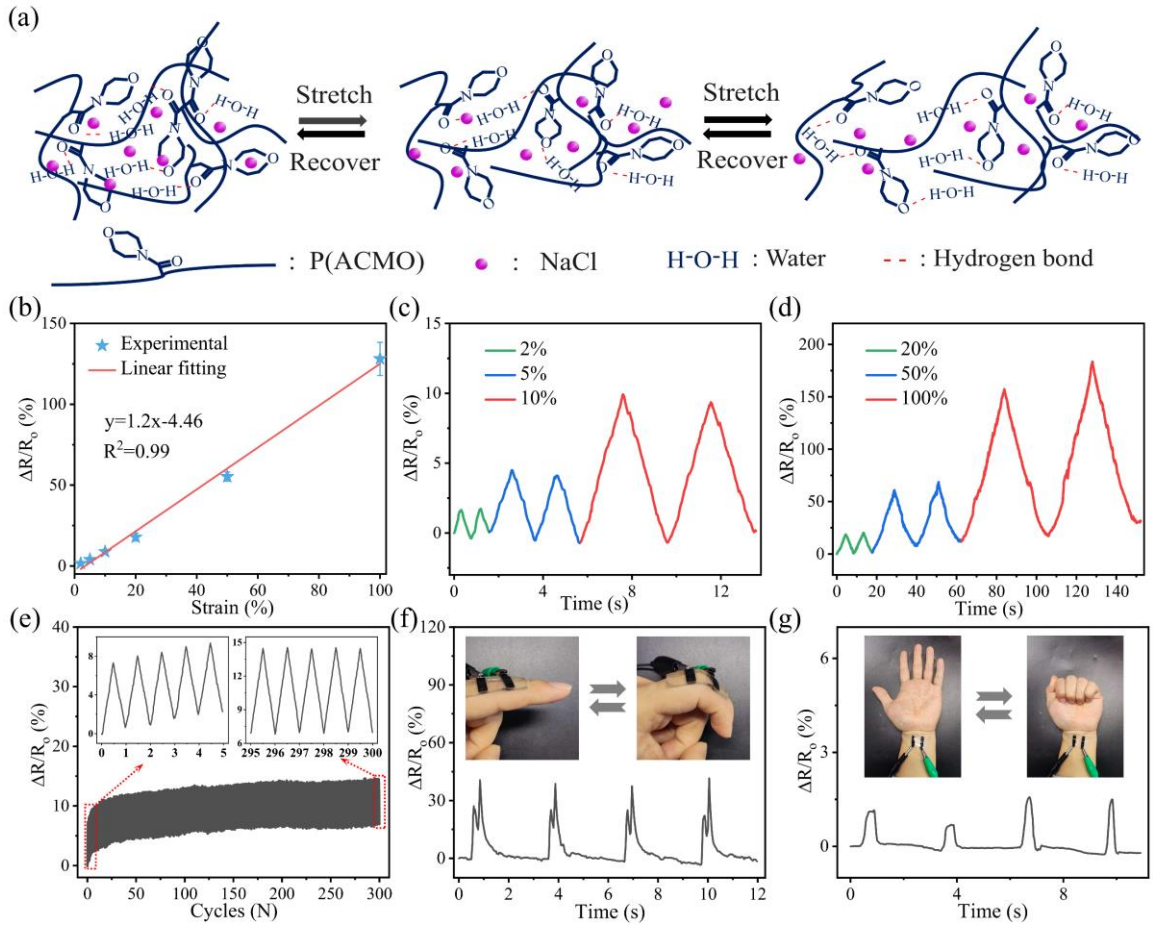

Figure 9. (a) Sensing mechanism of the P(ACMO)/NaCl hydrogel strain sensor. **(b)** Linear fitting of the $\Delta R/R_0$ of the P(ACMO)/NaCl sensor against the tensile strain within 0–100%. Resistance response of the P(ACMO)/NaCl sensor with **(c)** low and **(d)** large strains. **(e)** Resistance response of the P(ACMO)/NaCl sensor under a cyclic stretch-release test for 300 cycles at a 10% tensile strain. Images and resistance response of P(ACMO)/NaCl sensor attached to the **(f)** finger and **(g)** wrist.

Figure 9(a) illustrates the sensing mechanism of the P(ACMO)/NaCl hydrogel strain sensor. The resistance of the sensor was attributable to the energy barrier for ion migration, with higher energy barriers resulting in greater resistance. During deformation, as the length of the hydrogel increased and the cross-sectional area decreased, the energy barrier for ion migration heightened, leading to an increase in hydrogel resistance. As the hydrogel experienced greater strain, its resistance sharply increased. Upon stress release and the hydrogel returning to its initial state, the energy barrier for ion migration decreased, and the resistance returned to its initial value. To characterize the sensing properties of the P(ACMO)/NaCl sensor, a multimeter was used to measure the $\Delta R/R_0$ of the sensor at different strains. Figure 9(b) presents the linear fitting result of $\Delta R/R_0$ of the sensor against strain, with a gauge factor (GF) of 1.2. As depicted in Figures 9(c) and 9(d), the sensor exhibited excellent repeatability in response to both small strains of 2, 5, and 10%, as well as large strains of 20, 50, and 100%. Figure 9(e) illustrates the $\Delta R/R_0$ of the sensor during 300 cycles of stretching and recovery at a strain of 10%. It demonstrated stable and repeatable responses across different cycle numbers, showcasing excellent cycling stability.

Significantly, the P(ACMO)/NaCl hydrogel strain sensor was employed for monitoring human health conditions. Due to its adhesive properties based on 3M tape, the sensor could be attached to the surface of the human skin, including finger joints and wrist areas, as depicted in Figures 9(f) and 9(g). When periodic changes occurred in finger bending and wrist gripping, the $\Delta R/R_0$ of the sensor exhibited stable and repeatable responses. It could accurately monitor human motion behavior, demonstrating potential applications in medical monitoring.

For epidermal sensors, ensuring biocompatibility is essential for human health. The NIH-3T3 cell viability within the P(ACMO) hydrogel was assessed in vitro using a live/dead cell staining kit at different time intervals. As shown in Figure 10(a), the number of NIH-3T3 cells exhibiting green fluorescence increased progressively over time (from 1 to 3 and 7 days), indicating the promising biocompatibility of the P(ACMO) hydrogel.

Electronic devices with promising biodegradable properties are crucial for addressing global ecological challenges. Figure 10(b) illustrates the degradation process of DLP-printed P(ACMO) hydrogel compared to commercial flexible FLFLGR02 resin when placed in soil. Notably, the P(ACMO) hydrogel gradually broke down from bulk material into smaller fragments, eventually degrading completely within 15 days. In contrast, the flexible FLFLGR02 resin remained unchanged over time, indicating its non-degradable nature. The degradability of the P(ACMO) hydrogel ensures it won't persist in the environment, reducing long-term ecological harm. The combination of degradability and biocompatibility positions P(ACMO) hydrogel as a viable option for future sustainable electronics.

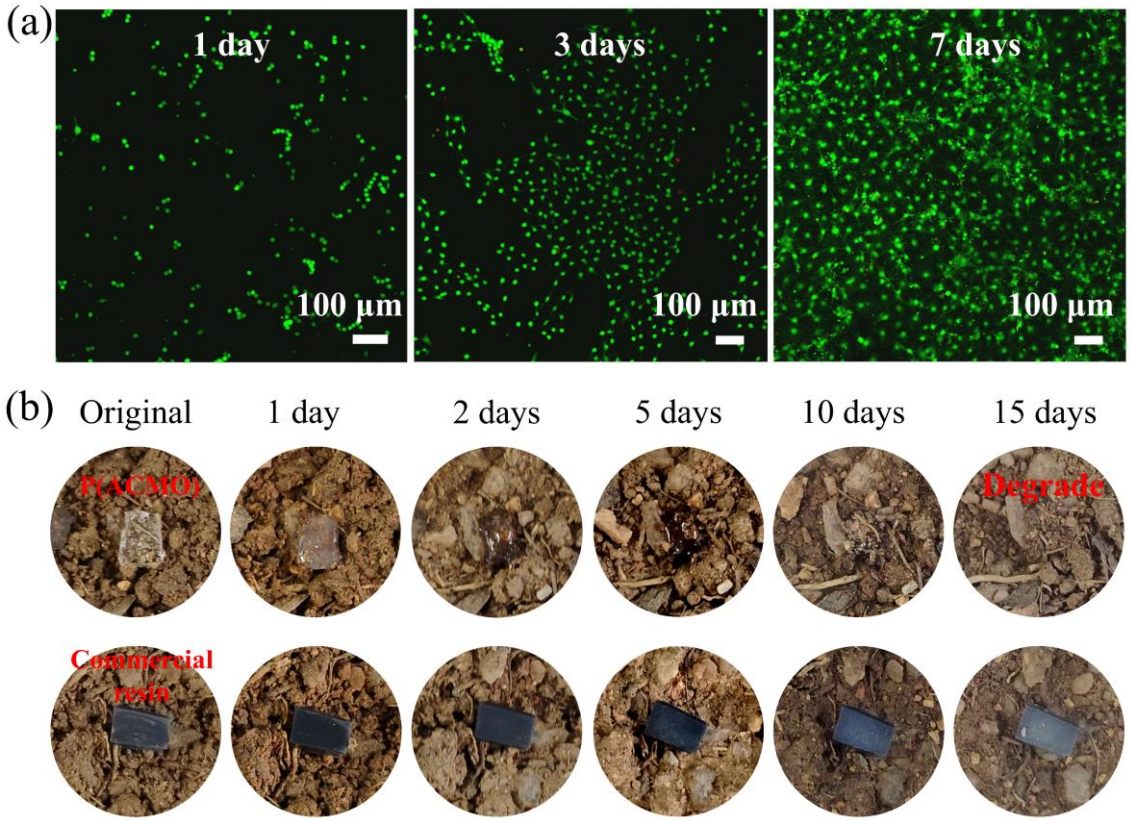

Figure 10. (a) Live/dead assay images of NIH-3T3 cells grown in P(ACMO)-enriched MEM Complete Medium at 1, 3, and 7 days. **(b)** The degradability of the P(ACMO) hydrogel in soil, with commercial flexible FLFLGR02 resin used for comparison.

4. Conclusions

In this study, we comprehensively compared the curing and rheological properties of the ACMO, HEMA, and PEGDA resins, as well as the water absorption behavior, mechanical characteristics, and tensile-fracture mechanisms of the corresponding hydrogels. Specifically, the printing duration of the P(ACMO) part was relatively short, requiring only 1.5 min. The reversible breaking and recombination of hydrogen bonds between P(ACMO) segments and water molecules endowed the P(ACMO) hydrogel with excellent mechanical stretchability. After determining the P(ACMO) hydrogel as the reliable substrate material, NaCl aqueous solution was sprayed to endow the hydrogel with promising ionic conductivity of 0.08 ± 0.016 S/m and GF of 1.2 at 0–100% strain. Additionally, good cycling stability and feasibility of monitoring human activities were obtained. Remarkably, the P(ACMO) hydrogel demonstrated notable biocompatibility and degradability, positioning it as a promising candidate for sustainable electronics in the future. This study proposed a new perspective on utilizing non-aqueous photopolymer resins for the rapid preparation of 3D printed ionically conductive hydrogels, providing instructive strategies for the next generation of flexible electronic devices.

Acknowledgments

This work was financially supported by the National Key R&D Program of China (2022YFE0197100) and Shenzhen Science and Technology Innovation Commission (GJHZ20200731095606021, KQTD20190929172505711, 20200925155544005). This research is also supported by MOE SUTD Kickstarter initiative (SKI 2021_02_16) and Singapore Ministry of Education academic research grant Tier 2 (MOE-T2EP50121-0007). The authors acknowledge the assistance of SUSTech Core Research Facilities.

Conflicts of Interests

No conflicts of interest were reported by any of the authors.

Authors' Contribution

Conceptualization, Binbin Guo and Xiaoteng Chen; methodology, Binbin Guo; software, Binbin Guo; validation, Binbin Guo and Xiaoteng Chen; formal analysis, Binbin Guo; investigation, Xiaoteng Chen; resources, Binbin Guo and Xiaoteng Chen; data curation, Binbin Guo; writing—original draft preparation, Binbin Guo and Xiaoteng Chen; writing—review and editing, Hui Ying Yang and Jiaming Bai; visualization, Hui Ying Yang; supervision, Hui Ying Yang and Jiaming Bai; project administration, Jiaming Bai; funding acquisition, Hui Ying Yang and Jiaming Bai. All authors have read and agreed to the published version of the manuscript.

References

[1] Yang C, Suo Z. Hydrogel ionotronics. *Nat. Rev. Mater.* 2018, 3(6):125–142.
[2] Tang Z, He H, Zhu L, Liu Z, Yang J, *et al.* A general protein unfolding-chemical coupling strategy for pure protein hydrogels with mechanically strong and multifunctional properties. *Adv. Sci.* 2022, 9(5):2102557.
[3] Zhang Y S, Khademhosseini A. Advances in engineering hydrogels. *Science.* 2017, 356(6337): eaaf3627.
[4] Azadi S, Peng S, Moshizi S A, Asadnia M, Xu J, *et al.* Biocompatible and highly stretchable PVA/AgNWs hydrogel strain sensors for human motion detection. *Adv. Mater. Technol.* 2020, 5(11):2000426.
[5] Liang Q, Xia X, Sun X, Yu D, Huang X, *et al.* Highly stretchable hydrogels as wearable and implantable sensors for recording physiological and brain neural signals. *Adv. Sci.* 2022, 9(16):2201059.
[6] Ricciardi R, Auriemma F, De Rosa C, Lauprêtre F. X-ray diffraction analysis of poly (vinyl alcohol) hydrogels, obtained by freezing and thawing techniques. *Macromolecules.* 2004, 37(5):1921–1927.
[7] Abudabbus M M, Jevremović I, Nešović K, Perić-Grujić A, Rhee K Y, *et al.* In situ electrochemical synthesis of silver-doped poly (vinyl alcohol)/graphene composite hydrogels and their physico-chemical and thermal properties. *Compos. Part B Eng*. 2018, 140:99–107.
[8] Guo B, Liang G, Yu S, Wang Y, Zhi C, *et al.* 3D printing of reduced graphene oxide aerogels for energy storage devices: a paradigm from materials and technologies to applications. *Energy Storage Mater.* 2021, 39:146–165.

[9] Guo B, Kang J, Zeng T, Qu H, Yu S, *et al.* 3D printing of multiscale Ti64-based lattice electrocatalysts for robust oxygen evolution reaction. *Adv. Sci.* 2022, 9(24):2201751.
[10] Ngo T D, Kashani A, Imbalzano G, Nguyen K T, Hui D. Additive manufacturing (3D printing): A review of materials, methods, applications and challenges. *Compos. Part B Eng*. 2018, 143:172–196.
[11] Tay Y W D, Panda B, Paul S C, Noor Mohamed N A, Tan M J, *et al.* 3D printing trends in building and construction industry: a review. *Virt. Phys. Prototyp*. 2017, 12(3):261–276.
[12] Guo B, Zhong Y, Chen X, Yu S, Bai J. 3D printing of electrically conductive and degradable hydrogel for epidermal strain sensor. *Compos. Commun.* 2023, 37:101454.
[13] Guo B, Zhong Y, Song X, Chen X, Zhou P, *et al.* 3D printing of mechanically elastic, self-adhesive, and biocompatible organohydrogels for wearable and breathable strain sensors. *Adv. Mater. Technol.* 2023, 8(5):2201078.
[14] Yin X Y, Zhang Y, Cai X, Guo Q, Yang J, *et al.* 3D printing of ionic conductors for high-sensitivity wearable sensors. *Mater. Horiz.* 2019, 6(4):767–780.
[15] Wang Z, Chen L, Chen Y, Liu P, Duan H, *et al.* 3D printed ultrastretchable, hyper-antifreezing conductive hydrogel for sensitive motion and electrophysiological signal monitoring. *Research*. 2020, 2020:1426078.
[16] Yan H, Zhou J, Wang C, Gong H, Liu W, *et al*. 3D printing of dual cross-linked hydrogel for fingerprint-like iontronic pressure sensor. *Smart Mater. Struct*. 2021, 31(1):015019.
[17] He Y, Yu R, Li X, Zhang M, Zhang Y, *et al*. Digital light processing 4D printing of transparent, strong, highly conductive hydrogels. *ACS Appl. Mater. Interfaces.* 2021, 13(30):36286–36294.
[18] Wu Y, Zeng Y, Chen Y, Li C, Qiu R, *et al*. Photocurable 3D printing of high toughness and self-healing hydrogels for customized wearable flexible sensors. *Adv. Funct. Mater.* 2021, 31(52):2107202.
[19] Wang Y, Spencer P, Yao X, Ye Q. Effect of coinitiator and water on the photoreactivity and photopolymerization of HEMA/camphoquinone-based reactant mixtures. *J. Biomed. Mater. Res. Part A*. 2006, 78(4):721–728.
[20] Dominguez-Alfaro A, Mitoudi-Vagourdi E, Dimov I, Picchio M L, Lopez-Larrea N, *et al.* Light-based 3D multi-material printing of micro-structured bio-shaped, conducting and dry adhesive electrodes for bioelectronics. *Adv. Sci.* 2024:2306424.
[21] Dou Y, Li S, Wang S, Gibril M E, Kong F. Utilizing methacrylated lignin as a sustainable macro-crosslinker for synthesizing innovative PVA/AMPS composites crosslinked hydrogel nanofibers: A potential application for lithium-ion battery separators. *Compos. Part B Eng*. 2024, 281:111537.
[22] Li Z, Chen Z, Liu J, Fu Y, Liu C, *et al.* Additive manufacturing of lightweight and high-strength polymer-derived SiOC ceramics. *Virtual Phys. Prototyp.* 2020, 15(2):163–177.
[23] Zhang G, Song D, Jiang J, Li W, Huang H, *et al.* Electrically assisted continuous vat photopolymerization 3D printing for fabricating high-performance ordered graphene/polymer composites. *Compos. Part B Eng*. 2023, 250:110449.
[24] Zhu G, Hou Y, Xu J, Zhao N. Reprintable polymers for digital light processing 3D printing. *Adv. Funct. Mater.* 2021, 31(9):2007173.
[25] Steiner T. The hydrogen bond in the solid state. *Angew. Chem. Int. Ed.* 2002, 41(1):48–76.
[26] Cai J, Ye D, Wu Y, Fan L, Yu H. Injectable alginate fibrous hydrogel with a three-dimensional network structure fabricated by microfluidic spinning. *Compos. Commun.* 2019, 15:1–5.
[27] Jeon S, Kim H, Choi J, Kim J F, Park H B, *et al.* Extreme pH-resistant, highly cation-selective poly (quaternary ammonium) membranes fabricated via menshutkin reaction-based interfacial polymerization. *Adv. Funct. Mater*. 2023, 33(22):2300183.
[28] Xu L, Huang Z, Deng Z, Du Z, Sun T L, *et al.* A transparent, highly stretchable, solvent-

resistant, recyclable multifunctional ionogel with underwater self-healing and adhesion for reliable strain sensors. *Adv. Mater*. 2021, 33(51):2105306.
[29] Ling Q, Liu W, Liu J, Zhao L, Ren Z, *et al*. Highly sensitive and robust polysaccharide-based composite hydrogel sensor integrated with underwater repeatable self-adhesion and rapid self-healing for human motion detection. *ACS Appl. Mater. Interfaces* 2022, 14(21):24741–24754.
[30] Gao Y, Gu S, Jia F, Gao G. A skin-matchable, recyclable and biofriendly strain sensor based on a hydrolyzed keratin-containing hydrogel. *J. Mater. Chem. A* 2020, 8(45):24175–24183.
[31] Song J H, Kim Y T, Cho S, Song W J, Moon S, *et al*. Surface-embedded stretchable electrodes by direct printing and their uses to fabricate ultrathin vibration sensors and circuits for 3D structures. *Adv. Mater.* 2017, 29(43):1702625.
[32] Xu F, Zhu Y. Highly conductive and stretchable silver nanowire conductors. *Adv. Mater.* 2012, 24(37):5117–5122.